Electronic Supplementary Material (ESI) for Journal of Materials Chemistry A

Supporting Information

Metallocene/carbon hybrids prepared by a solution process for supercapacitor applications

Xianwen Mao, Fritz Simeon, Demetra S. Achilleos, Gregory C. Rutledge, and T. Alan Hatton**

Department of Chemical Engineering, Massachusetts Institute of Technology
77 Massachusetts Avenue, Cambridge
Massachusetts, 02139, USA
E-mail: tahatton@mit.edu, rutledge@mit.edu

Index for this document

S1 Methods

S1.1 Materials

Polyvinylferrocene (PVF, molecular weight = 50,000 g/mol) was obtained from Polysciences and used as received. Multi-walled carbon nanotubes (CNTs) with a diameter of 6 to 9 nm and purity of 95% were obtained from Sigma Aldrich, and were used as received throughout the study, without further purification or chemical modification unless otherwise noted.

S1.2 Fabrication of PVF/CNT hybrids

PVF and CNTs in appropriate amounts were dissolved and dispersed in anhydrous chloroform via bath sonication for 45 min at room temperature. The resulting PVF/CNT ink was deposited into an O-ring with a diameter of ~0.6 cm on a solid substrate, and then dried in a vacuum oven at 50 °C for 30 min to remove the solvent completely. To test the electrochemical properties of the hybrids, PVF/CNT inks of various compositions (the total concentration was 1.25 mg mL^{-1}) were deposited onto conductive Toray carbon papers cut into sizes of 1 cm × 2 cm. The surface area of the Toray carbon paper electrode exposed to the electrolyte solution was controlled to be 1 cm × 1 cm by using epoxy to mask off part of the electrode.

S1.3 Microstructural characterization

Transmission electron microscopy (TEM) (JEOL-2010), scanning electron microscopy (SEM) (JOEL-6060 for general imaging and JOEL-6700 for high-resolution imaging), and atomic force microscopy (AFM) (Veeco, Nanoscope V with Dimension

3100) were used to investigate the morphologies of the PVF/CNT hybrids. X-ray photoelectron spectroscopy (XPS, Kratos Analytical) measurements were recorded with a Kratos Axis Ultra instrument equipped with a monochromatic Al Kα source operated at 150 W. The analyzer angle was set at 90° with respect to the specimen surface. Survey scan spectra were recorded over a binding energy range of 0-1100 eV and pass energy of 160 eV. Raman spectra were recorded with a Horiba Jobin Yvon Labram HR800 spectrometer using a 633 nm laser source. X-ray diffraction (XRD) patterns were recorded using a Bruker AXS Diffractometer with Cu/Co radiation at the scanning speed of 0.62°/min between 5° and 60° (2θ). Ultraviolet photoemission spectra (UPS) were obtained using a He(I) emission lamp (21.20 eV photon energy) and collected at a 0.01 eV resolution with an electron take-off angle of 90° and a pass energy of 0.585 eV. The surface areas were determined from nitrogen adsorption isotherms (ASAP2020, Micromeritics) by means of the Brunauer−Emmett−Teller (BET) method.

S1.4 Electrochemical measurements

Electrochemical experiments were performed using an AutoLab PGSTAT 30 potentiostat with GPES software.

S1.4.1 Three-electrode tests

When a three-electrode configuration was employed, a platinum wire and a Ag/AgCl (3 M NaCl) electrode (BASi) were used as the auxiliary and reference electrodes, respectively. All potentials are referred to the Ag/AgCl electrode. The auxiliary and reference electrodes were rinsed with ethanol followed by ultrapure water before each experiment. The electrolyte was 0.5 M $NaClO_4$.

S1.4.2 Two-electrode tests

For construction of supercapacitor devices, two pieces of PVF_{80}/CNT_{20}-deposited Toray carbon papers were assembled with a filter paper (VWR) sandwiched between them as the separator. The total mass of the active materials on one electrode was 750 μg. The thickness of the PVF_{80}/CNT_{20} layer on one side was ~22 μm (which is larger than the recommended thickness of 15 μm for commercial supercapacitors), with nominal area of ~0.28 cm^2, controlled by an O-ring with a diameter of ~0.6 cm. The electrolyte for the supercapacitor device was either 0.5 M $NaClO_4$ or 1 M H_2SO_4.

S1.4.3 Calculation of specific capacitance from cyclic voltammograms

In a three-electrode configuration, the specific capacitance was calculated from the cyclic voltammogram according to the following equation:[1]

$$C = \int_{V_1}^{V_2} [i_a(V) - i_c(V)]dV \Big/ [2(V_2 - V_1)mv] \quad (1)$$

where C is the gravimetric capacitance of the sample, V_1 and V_2 are the cutoff potentials in cyclic voltammetry, $i_a(V)$ and $i_c(V)$ are the instantaneous anodic and cathodic currents as a function of potential, v is the scan rate, and m is the total mass of the active materials on one electrode. In a two-electrode configuration, m is the total mass of the active materials on both electrodes, and the expression in (1) is multiplied by a factor of four, which adjusts the capacitance of the cell and the combined mass of two electrodes to the capacitance and mass of a single electrode.[2] Equation (1) is a universal expression that applies to cyclic voltammograms of any shape since it uses the integral area of the cyclic voltammogram/scan rate to represent the sum of anodic and cathodic voltammetric charges.[1]

S1.4.4 Calculation of specific capacitance, energy density, and power density from galvanostatic measurements

The specific capacitance from the galvanostatic measurements can be calculated by the equation:[3]

$$C = I\Delta t / (m\Delta V) \quad (2)$$

where I is the discharge current, Δt is the discharge time, ΔV is the voltage change, and m is the mass of the active material. In a two-electrode configuration, m is the total mass of the active material on both electrodes. The energy density was estimated based on the two-electrode configuration either by using the capacitance value:

$$E = \frac{1}{2} C_{2-electrode} V^2 \quad (3)$$

where $C_{2-electrode}$ is the specific capacitance obtained in a two-electrode configuration, and V is the voltage change during the discharge process, or by using the integration method:

$$E = i \times \int V(t) dt \quad (4)$$

where i is the discharge current density and $V(t)$ is the instantaneous voltage as a function of time. An effective series resistance (ESR), R_{ESR}, was estimated using the voltage drop at the beginning of the discharge, V_{drop}, at a certain current density, I, with the formula:

$$R_{ESR} = \frac{V_{drop}}{2I} \quad (5)$$

The power density, calculated from the discharge data at a certain current density and normalized with the total mass of the active materials on both electrodes, m, is given by

$$P = \frac{\left(V - V_{drop}\right)^2}{4R_{ESR}m} \tag{6}$$

S1.5 Calculation of the Fe/C ratio from XPS

To obtain the Fe/C ratios for different samples, their XPS survey scans were analyzed using the CasaXPS software. Energy calibration for the XPS survey scans was performed by setting the peak position of the carbon line to 284.0 eV. The quantification regions to calculate the atomic concentration of the C and Fe elements were 275 – 295 eV and 700 – 712 eV, respectively. Shirley background types[4] were selected for the quantification regions in order to obtain smooth baselines.

S1.6 Determination of ferrocene utilization efficiency using chronocoulometry

We carried out chronocoulometry measurements for PVF_{80}/CNT_{20} and pure CNTs at different oxidation potentials from 0.2 to 0.7 V versus Ag/AgCl (**Figure S1a and S1b**). The ferrocene utilization efficiency is calculated by subtracting the charge observed with CNTs alone (as shown in **Figure S1b**) from the total charge observed with PVF_{80}/CNT_{20} (as shown in **Figure S1a**), and then dividing the difference (i.e., the net charge solely due to PVF oxidation) by the theoretical value that would be obtained if all ferrocenes were to be oxidized (i.e., 100% efficiency). Specifically, it can be calculated according to the equation:

$$U = \frac{Q_{total}(C/g) - Q_{CNT}(C/g) f_{CNT}}{f_{PVF} Q_{theoretical}(C/g)} \times 100\% \tag{7}$$

where U is the ferrocene utilization efficiency, Q_{total} is the total charge of PVF_{80}/CNT_{20} as shown in **Figure S1a**, Q_{CNT} is the charge of CNTs alone as shown in **Figure S1b**, f_{CNT} and f_{PVF} are the weight fractions of CNTs and PVF in the PVF/CNT hybrid, respectively, and $Q_{theoretical}$ is the value that would be attained if all the ferrocenes were to be oxidized. With increasing potentials, the ferrocene utilization efficiency increases due to the enhanced oxidation level. We observed that from 0.6 to 0.7 V, the ferrocene utilization efficiency increased only marginally, indicating that at 0.6 V PVF might have already reached its oxidation limit. Therefore, we compared the ferrocene utilization efficiency for PVF_{80}/CNT_{20} with that of PVF at 0.6 V as shown in **Figure S2**.

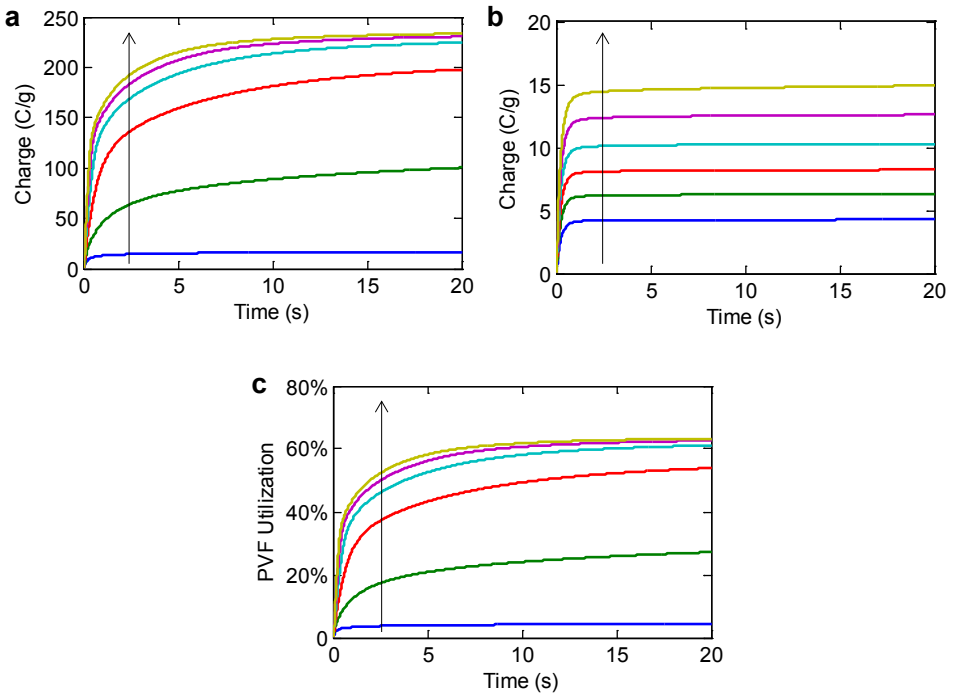

Figure S1. (a-b) Chronocoulometry measurements for (a) PVF_{80}/CNT_{20}, and (b) untreated CNTs. (c) The calculated PVF utilizations as a function of time for

PVF_{80}/CNT_{20}. With the arrow direction, the potential was stepped from 0 V to 0.2, 0.3, 0.4, 0.5, 0.6 and 0.7 V.

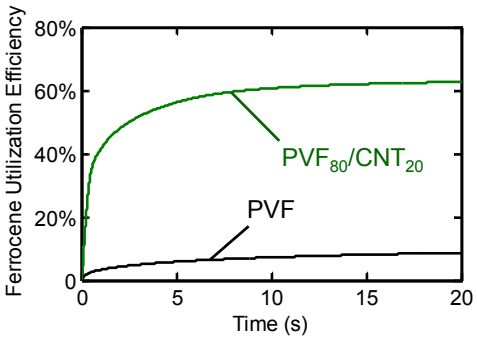

Figure S2. Ferrocene utilization efficiency as a function of oxidation time for PVF_{80}/CNT_{20} and PVF. The plateau efficiency values for PVF_{80}/CNT_{20} and PVF are 63% and 8%, respectively.

S1.7 Determination of charging resistance from electrochemical impedance spectroscopy (EIS)

Charging resistance at a certain frequency corresponds to the real part of the impedance in the Nyquist plot (i.e., the EIS spectra, **Figure S3**) minus the high frequency resistance (at 10^4 Hz).[5-7] The EIS spectra were obtained at a potential of 0.5 V in the frequency range of 10000 Hz to 10 Hz in 0.5 M $NaClO_4$. An alternating sinusoidal signal of 50 mV peak-to-peak was superimposed on the *dc*-potential. The corresponding charging resistances for PVF_{80}/CNT_{20} and PVF are shown in Figure S4. It can be clearly seen that the charging resistance for PVF_{80}/CNT_{20} is much lower than that for PVF.

The charging resistances at other oxidation levels (0.3, 0.4, and 0.6 V) are shown in **Figure S5**, and no significant difference across different potentials is observed.

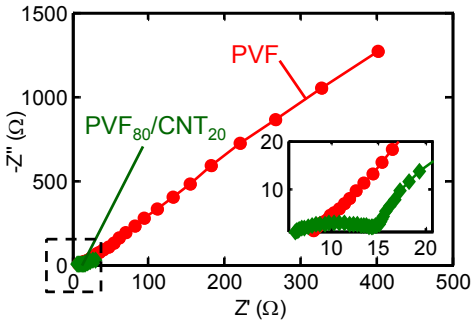

Figure S3. The Nyquist plot for PVF and PVF_{80}/CNT_{20} determined by electrochemical impedance spectroscopy at an oxidation level of 0.5 V. Inset: magnification of the dotted rectangle.

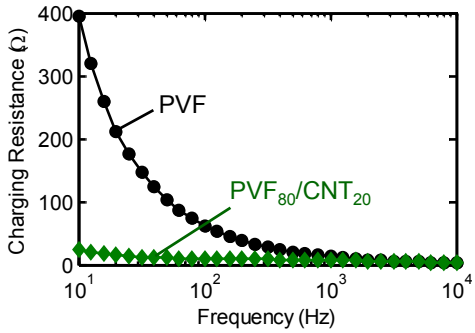

Figure S4. The calculated charging resistance as a function of frequency for PVF and PVF_{80}/CNT_{20}.

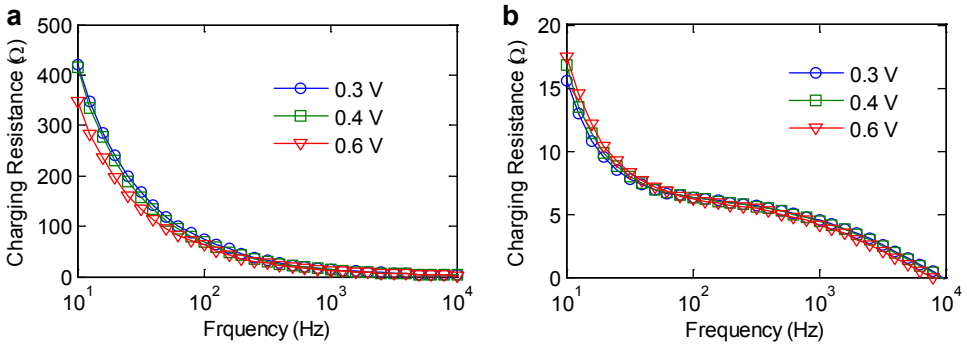

Figure S5. The calculated charging resistance at other potentials (0.3, 0.4, and 0.6 V) as a function of frequency for (a) PVF, and (b) PVF_{80}/CNT_{20}.

S1.8 Calculation of the I_D/I_G ratio from Raman spectra

The Raman spectra were analyzed using the LabSpec 5 software. The baseline correction of the spectra was implemented using a polynomial with a degree of seven. The D and G peaks were fitted using a Gaussian-Lorentzian mixed shape. The fitting results are summarized in **Figure S6** and **Table S1**.

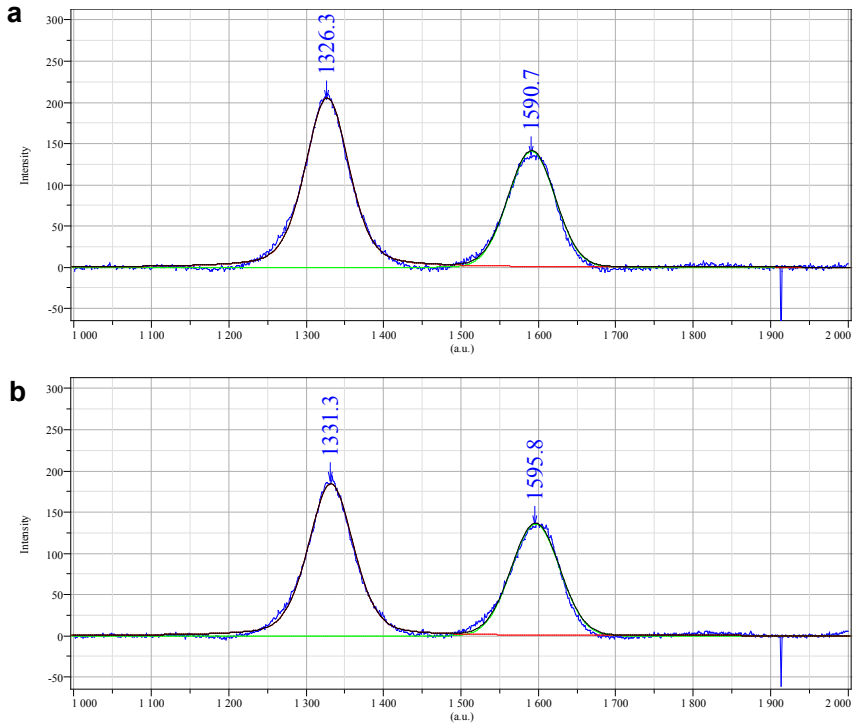

Figure S6. Raman spectra with superposition of the two fitted Gaussian-Lorentzian peaks for (a) pristine CNTs and (b) PVF_{80}/CNT_{20}.

Table S1. D band frequency (ν_D), D band full width at half maximum (D^{FWHM}), G band frequency (ν_G), G band full width at half maximum (G^{FWHM}), and I_D/I_G ratio for pristine CNTs and PVF_{80}/CNT_{20}.

	ν_D (cm^{-1})	D^{FWHM} (cm^{-1})	ν_G (cm^{-1})	G^{FWHM} (cm^{-1})	I_D/I_G
Pristine CNTs	1326.3	65.8	1590.7	71.1	1.4
PVF_{80}/CNT_{20}	1331.3	67.9	1595.8	73.8	1.4

S1.9 Calculation of the work functions from ultraviolet photoelectron spectra (UPS)

The work function (ϕ) is determined by $\phi = E_{photon} - E_{HBC}$,[8-10] where E_{photon} is the incident photon energy, 21.20 eV, and E_{HBC} is the high binding energy cutoff, determined by extrapolating the high binding energy linear regime of the UPS spectra to zero intensity. Because the UPS results are often sensitive to surface morphology or surface roughness, we took spectra from three different locations on the sample surfaces to ensure the spectra acquired were reliable and consistent. The high binding energy regimes of UPS spectra for pristine CNTs and PVF_{80}/CNT_{20} obtained at different locations are shown in **Figure S7**. The linear fitting range for pristine CNTs is from 16.7 to 17 eV (indicated by the red rectangle), which results in three values of $E_{HBC,CNT}$ equal to 17.26, 17.26 and 17.22 eV. The linear fitting range for PVF_{80}/CNT_{20} is from 15.8 to 16.4 eV (indicated by the green rectangle), which results in three values of $E_{HBC,PVF/CNT}$ equal to 16.68, 16.58 and 16.69 eV. The work functions were then calculated according to the equation $\phi = E_{photon} - E_{HBC}$. The work functions for pristine CNTs at three different spots were 3.94, 3.94, and 3.98 eV, giving rise to an average value of 3.95 ± 0.02 eV (s.d.). The work functions for PVF_{80}/CNT_{20} at three different spots were 4.51, 4.62, and 4.50 eV, giving rise to an average value of 4.54 ± 0.06 eV (s.d.).

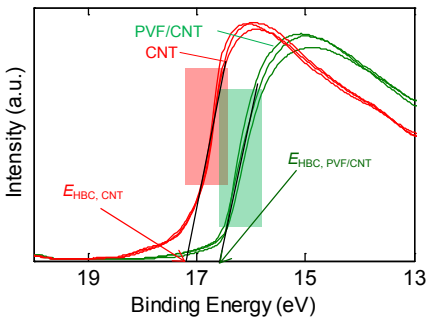

Figure S7. The high binding energy regimes of the ultraviolet photoelectron spectra for pristine CNTs and PVF_{80}/CNT_{20} obtained at three different spots.

S2 Supplementary tables and figures

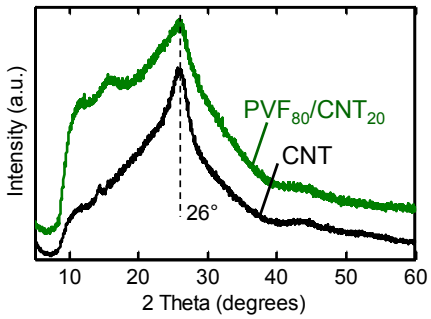

Figure S8. X-ray diffraction (XRD) patterns for PVF_{80}/CNT_{20} and pristine CNTs as a control. Both samples display a characteristic peak at 2θ = 26°, corresponding to diffraction from the graphite-like lattices of these multi-walled CNTs.[11, 12] This suggests that the lattice structure of the nanotube component is not destroyed in the preparation of PVF_{80}/CNT_{20}.

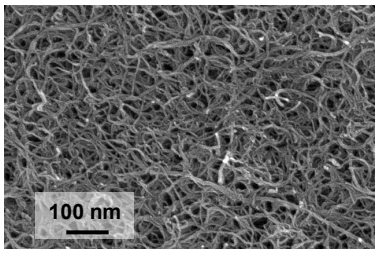

Figure S9. High-resolution scanning electron microscopy (HR-SEM) image of the deposited un-modified CNTs.

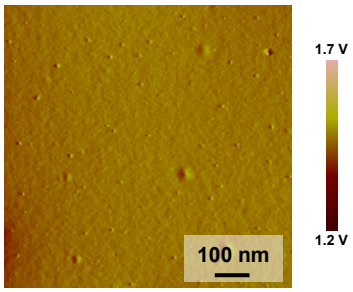

Figure S10. Atomic force microscopy (AFM) amplitude image of a pure PVF film deposited on a silicon wafer.

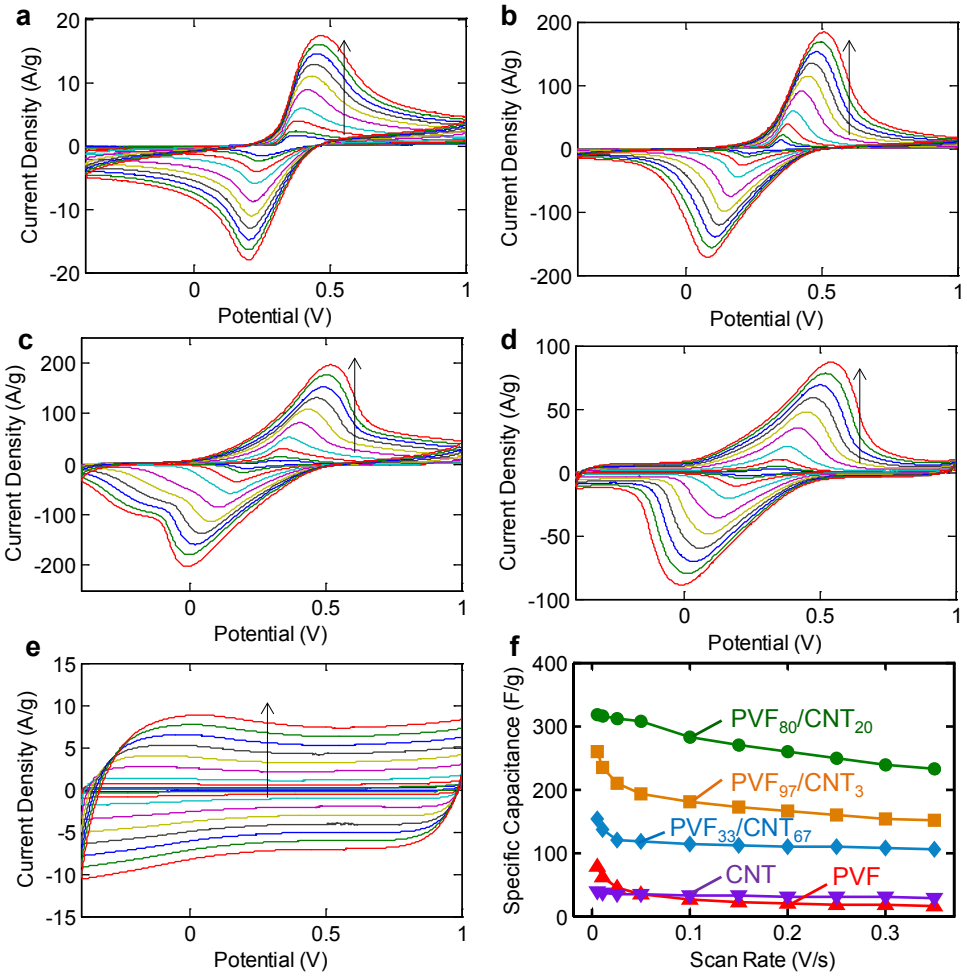

Figure S11. (a – e) Cyclic voltammograms at different scan rates for (a) PVF alone, (b) PVF_{97}/CNT_3, (c) PVF_{80}/CNT_{20}, (d) PVF_{33}/CNT_{67}, and (e) pristine CNTs. With the

arrow direction, the scan rates are 5, 10, 25, 50, 100, 150, 200, 250, 300, and 350 mV s^{-1}. The electrolyte solution was 0.5 M $NaClO_4$. (f) Specific capacitance versus scan rate, calculated from the cyclic voltammetric measurements.

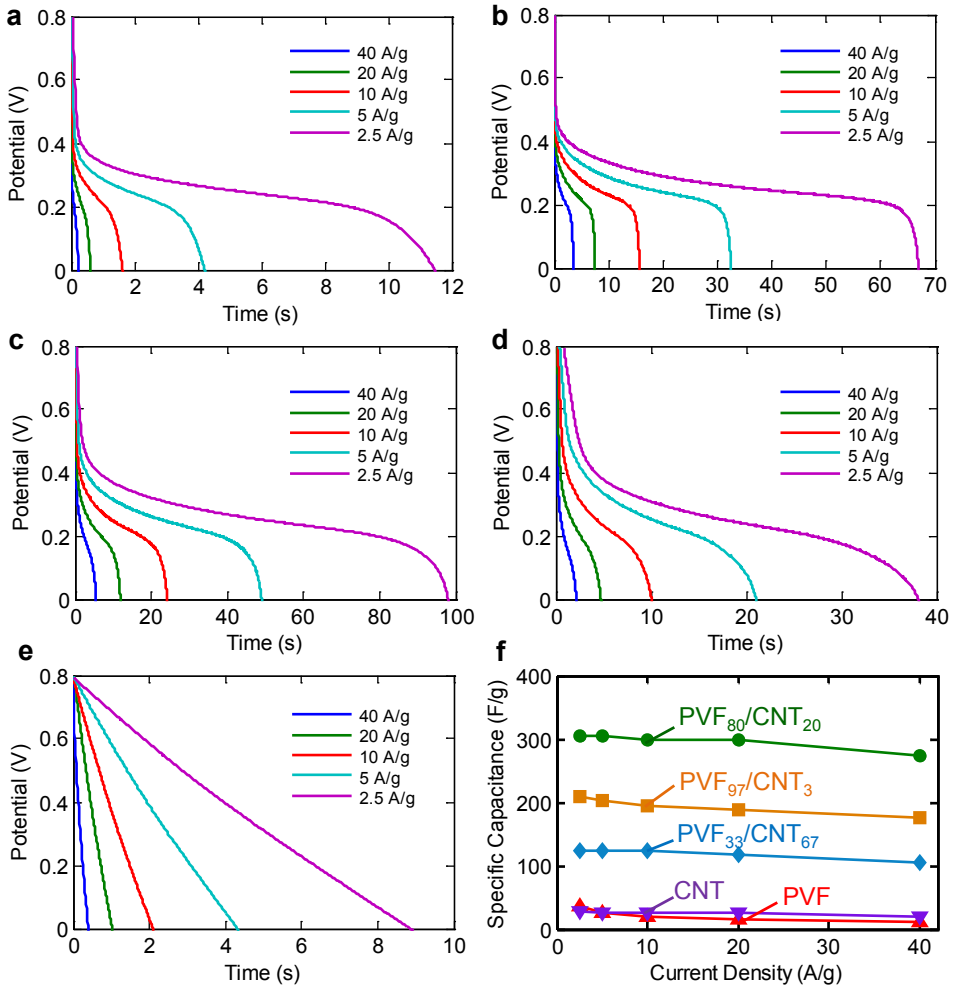

Figure S12. (a – e) Galvanostatic discharge profiles at different current densities for (a) PVF alone, (b) PVF_{97}/CNT_3, (c) PVF_{80}/CNT_{20}, (d) PVF_{33}/CNT_{67}, and (e) pristine CNTs. The electrolyte solution was 0.5 M $NaClO_4$. (f) Specific capacitance versus current density, calculated from the galvanostatic measurements.

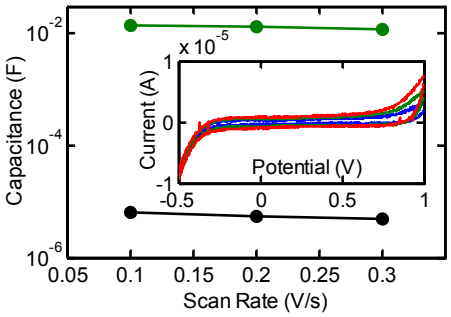

Figure S13. Comparison of the capacitance between a blank 1cm×1cm substrate (black) and a PVF_{80}/CNT_{20} (62.5 μg)-deposited substrate (green). Inset shows the cyclic voltammograms of a blank substrate at 0.1 (blue), 0.2 (green), and 0.3 (red) V/s. The blank substrate contributed less than 0.1% of the total capacitance of a PVF_{80}/CNT_{20}-deposited substrate. This indicates that the substrate had negligible effect on the electrochemical measurements of the PVF/CNT hybrid.

Table S2. Comparison of capacitance, energy density and power density for different pseudocapacitive materials.

Active materials	Capacitance[a] (F/g)	Energy Density (Wh/kg)	Power Density (kW/kg)	Electrolyte	Cell Configuration
PVF_{80}/CNT_{20} (this work)	1241@20 mV/s, 1452@20 A/g	79.5	16.6	1 M H_2SO_4	2-electrode
Poly(3,4-propylenedioxypyrrole)/CNT[13]	30	4.2	0.75	Gel electrolyte	3-electrode
PANI/CNT[14]	1030@5.9 A/g	-	-	1 M H_2SO_4	3-electrode
PANI/graphene[15]	970@2.5 A/g	-	-	1 M Na_2SO_4	3-electrode
PANI/porous carbon[16]	2200@0.67 A/g[b]	300[b]	0.47[b]	1 M H_2SO_4	3-electrode
PANI/graphene[17]	233	-	-	1 M H_2SO_4	3-electrode
PANI/mesoporous carbon[18]	900@0.5 A/g			1 M H_2SO_4	3-electrode
MnO_2/poly(3,4-ethylenedioxythi	210	-	-	1 M Na_2SO_4	2-electrode

ophene)[19]					
PANI/amine-modified graphene[20]	330@20 mV/s, 388@1 A/g	9.6	-	1 M H_2SO_4	3-electrode
PPY/carbon aerogel[21]	433@1 mV/s	-	-	6 M KOH	3-electrode
PPY/CNT[22]	192@5 mV/s, 200@0.25 A/g	-	-	1 M H_2SO_4	2-electrode
PANI/CNT[22]	344@2 mV/s, 360@0.2 A/g	-	-	1 M H_2SO_4	2-electrode
PPY/graphene[23]	267@10 mV/s	-	-	1 M KCl	3-electrode
PPY/carbon nanocoil[24]	193@5 mV/s, 200@2.5 A/g	-	-	1 M H_2SO_4	2-electrode
PANI/carbon nanocoil[24]	354@1 mV/s, 325@2.5 A/g	44.61	-	1 M H_2SO_4	2-electrode
PANI/carbon nanofiber[25]	265@5 mV/s	-	-	1 M H_2SO_4	3-electrode
PANI/activated carbon[26]	273@50 mV/s	-	-	1 M H_2SO_4	3-electrode
PPY/graphene[27]	267@100 mV/s	-	-	1 M H_2SO_4	3-electrode
PANI/methyl orange/activated carbon[28]	390@10 mV/s, 219@0.2 A/g	-	-	1 M H_2SO_4	3-electrode
PANI hydrogel[29]	420@5 A/g	-	-	1 M H_2SO_4	3-electrode
PANI/porous graphene[30]	716@0.47 A/g	-	-	aqueous	3-electrode
PANI nanofiber/graphene[31]	210@0.3 A/g	~19	~0.2	1 M H_2SO_4	2-electrode
PANI/graphene[32]	554@0.2 A/g	-	-	1 M H_2SO_4	2-electrode
Brush-like Co_3O_4[33]	911@0.25 A/g	81	71	KOH	2-electrode
Co_3O_4 twin-sphere[34]	781@0.5 A/g	-	-	6 M KOH	3-electrode
Nanoporous RuO_2[35]	385@1 mV/s	-	-	1 M H_2SO_4	3-electrode
MnO_2/graphene/ conductive wrapping[36]	380	-	-	0.5 M Na_2SO_4	3-electrode
$Ni(OH)_2$/CNT[37]	3300	50.6	0.095	KOH	3-electrode
Manganese oxide/CNT[38]	199	-	-	1 M Na_2SO_4	3-electrode
MnO_2/CNT[39]	410@5 mV/s	~5-20	~13	0.5 M Na_2SO_4	3-electrode

Nickel-cobalt double hydroxides/zinc tin oxide[40]	1275@100 A/g	9.7	5.8	2 M KOH	3-electrode
MnO_2/nanoporous gold[41]	1145@50 mV/s	~57	~16	2 M $LiClO_4$	2-electrode
Co_3O_4/Ni[42]	1471@10 A/g	-	-	2 M KOH	3-electrode
MnO_2/Mn/MnO_2[43]	937@5 mV/s, 955@1.5 A/g	~52	~15	1 M Na_2SO_4	3-electrode

Notes for the table: (abbreviations) PANI: polyaniline; PPY polypyrrole. [a] The specific capacitance was calculated based on the total mass of the active materials, including all the components indicated in the first column of the table. [b] This value was not based on the total mass of PANI and carbon. Instead, it was calculated based on the mass of PANI only.

S3 References for the Supporting Information

[1] W. Chen, Z. L. Fan, L. Gu, X. H. Bao, C. L. Wang, *Chem Commun* **2010**, *46*, 3905.
[2] M. D. Stoller, R. S. Ruoff, *Energ Environ Sci* **2010**, *3*, 1294.
[3] Z. B. Lei, L. Lu, X. S. Zhao, *Energ Environ Sci* **2012**, *5*, 6391.
[4] H. Estrade-Szwarckopf, *Carbon* **2004**, *42*, 1713.
[5] B. H. Park, J. H. Choi, *Electrochim Acta* **2010**, *55*, 2888.
[6] H. Probstle, C. Schmitt, J. Fricke, *J Power Sources* **2002**, *105*, 189.
[7] H. Probstle, M. Wiener, J. Fricke, *J Porous Mat* **2003**, *10*, 213.
[8] P. E. Colavita, B. Sun, X. Y. Wang, R. J. Hamers, *J Phys Chem C* **2009**, *113*, 1526.
[9] J. D. Wiggins-Camacho, K. J. Stevenson, *J Phys Chem C* **2009**, *113*, 19082.
[10] E. C. Landis, K. L. Klein, A. Liao, E. Pop, D. K. Hensley, A. V. Melechko, R. J. Hamers, *Chem Mater* **2010**, *22*, 2357.
[11] X. T. Zhang, J. R. Liu, B. Xu, Y. F. Su, Y. J. Luo, *Carbon* **2011**, *49*, 1884.
[12] X. Zhang, J. Zhang, Z. Liu, *Appl Phys A-Mater* **2005**, *80*, 1813.
[13] M. Ertas, R. M. Walczak, R. K. Das, A. G. Rinzler, J. R. Reynolds, *Chem Mater* **2012**, *24*, 433.
[14] H. Zhang, G. Cao, Z. Wang, Y. Yang, Z. Shi, Z. Gu, *Electrochem Commun* **2008**, *10*, 1056.
[15] M. A. Q. Xue, F. W. Li, J. Zhu, H. Song, M. N. Zhang, T. B. Cao, *Adv Funct Mater* **2012**, *22*, 1284.
[16] L. Z. Fan, Y. S. Hu, J. Maier, P. Adelhelm, B. Smarsly, M. Antonietti, *Adv Funct Mater* **2007**, *17*, 3083.
[17] D.-W. Wang, F. Li, J. Zhao, W. Ren, Z.-G. Chen, J. Tan, Z.-S. Wu, I. Gentle, G. Q. Lu, H.-M. Cheng, *Acs Nano* **2009**, *3*, 1745.

[18] Y. G. Wang, H. Q. Li, Y. Y. Xia, *Adv Mater* **2006**, *18*, 2619.
[19] R. Liu, S. B. Lee, *J Am Chem Soc* **2008**, *130*, 2942.
[20] L. F. Lai, H. P. Yang, L. Wang, B. K. Teh, J. Q. Zhong, H. Chou, L. W. Chen, W. Chen, Z. X. Shen, R. S. Ruoff, J. Y. Lin, *Acs Nano* **2012**, *6*, 5941.
[21] H. F. An, Y. Wang, X. Y. Wang, L. P. Zheng, X. Y. Wang, L. H. Yi, L. Bai, X. Y. Zhang, *J Power Sources* **2010**, *195*, 6964.
[22] K. V, E. Frackowiak, F. Beguin, *Electrochim Acta* **2005**, *50*, 2499.
[23] A. Davies, P. Audette, B. Farrow, F. Hassan, Z. W. Chen, J. Y. Choi, A. P. Yu, *J Phys Chem C* **2011**, *115*, 17612.
[24] R. B. Rakhi, W. Chen, H. N. Alshareef, *Journal of Materials Chemistry* **2012**, *22*, 5177.
[25] J. Jang, J. Bae, M. Choi, S. H. Yoon, *Carbon* **2005**, *43*, 2730.
[26] K. S. Ryu, Y. G. Lee, K. M. Kim, Y. J. Park, Y. S. Hong, X. L. Wu, M. G. Kang, N. G. Park, R. Y. Song, J. M. Ko, *Synthetic Met* **2005**, *153*, 89.
[27] S. Bose, N. H. Kim, T. Kuila, K. T. Lau, J. H. Lee, *Nanotechnology* **2011**, *22*.
[28] Y. J. Jia, J. C. Jiang, K. Sun, T. Y. Dai, *Electrochim Acta* **2012**, *71*, 213.
[29] L. J. Pan, G. H. Yu, D. Y. Zhai, H. R. Lee, W. T. Zhao, N. Liu, H. L. Wang, B. C. K. Tee, Y. Shi, Y. Cui, Z. N. Bao, *Proc Natl Acad Sci U S A* **2012**, *109*, 9287.
[30] K. W. Chen, L. B. Chen, Y. Q. Chen, H. Bai, L. Li, *Journal of Materials Chemistry* **2012**, *22*, 20968.
[31] Q. Wu, Y. X. Xu, Z. Y. Yao, A. R. Liu, G. Q. Shi, *Acs Nano* **2010**, *4*, 1963.
[32] J. J. Xu, K. Wang, S. Z. Zu, B. H. Han, Z. X. Wei, *Acs Nano* **2010**, *4*, 5019.
[33] R. B. Rakhi, W. Chen, D. Y. Cha, H. N. Alshareef, *Nano Lett* **2012**, *12*, 2559.
[34] Y. H. Xiao, S. J. Liu, F. Li, A. Q. Zhang, J. H. Zhao, S. M. Fang, D. Z. Jia, *Adv Funct Mater* **2012**, *22*, 4052.
[35] Y. S. Hu, Y. G. Guo, W. Sigle, S. Hore, P. Balaya, J. Maier, *Nat Mater* **2006**, *5*, 713.
[36] G. H. Yu, L. B. Hu, N. A. Liu, H. L. Wang, M. Vosgueritchian, Y. Yang, Y. Cui, Z. A. Bao, *Nano Lett* **2011**, *11*, 4438.
[37] Z. Tang, C. H. Tang, H. Gong, *Adv Funct Mater* **2012**, *22*, 1272.
[38] H. Zhang, G. P. Cao, Z. Y. Wang, Y. S. Yang, Z. J. Shi, Z. N. Gu, *Nano Lett* **2008**, *8*, 2664.
[39] L. B. Hu, W. Chen, X. Xie, N. A. Liu, Y. Yang, H. Wu, Y. Yao, M. Pasta, H. N. Alshareef, Y. Cui, *Acs Nano* **2011**, *5*, 8904.
[40] X. Wang, A. Sumboja, M. F. Lin, J. Yan, P. S. Lee, *Nanoscale* **2012**, *4*, 7266.
[41] X. Y. Lang, A. Hirata, T. Fujita, M. W. Chen, *Nat Nanotechnol* **2011**, *6*, 232.
[42] C. Z. Yuan, L. Yang, L. R. Hou, L. F. Shen, X. G. Zhang, X. W. Lou, *Energ Environ Sci* **2012**, *5*, 7883.
[43] Q. Li, Z. L. Wang, G. R. Li, R. Guo, L. X. Ding, Y. X. Tong, *Nano Lett* **2012**, *12*, 3803.